FUNDAMENTALS & APPLICATIONS

CHEMELECTROCHEM

ANALYSIS & CATALYSIS, BIO & NANO, ENERGY & MORE

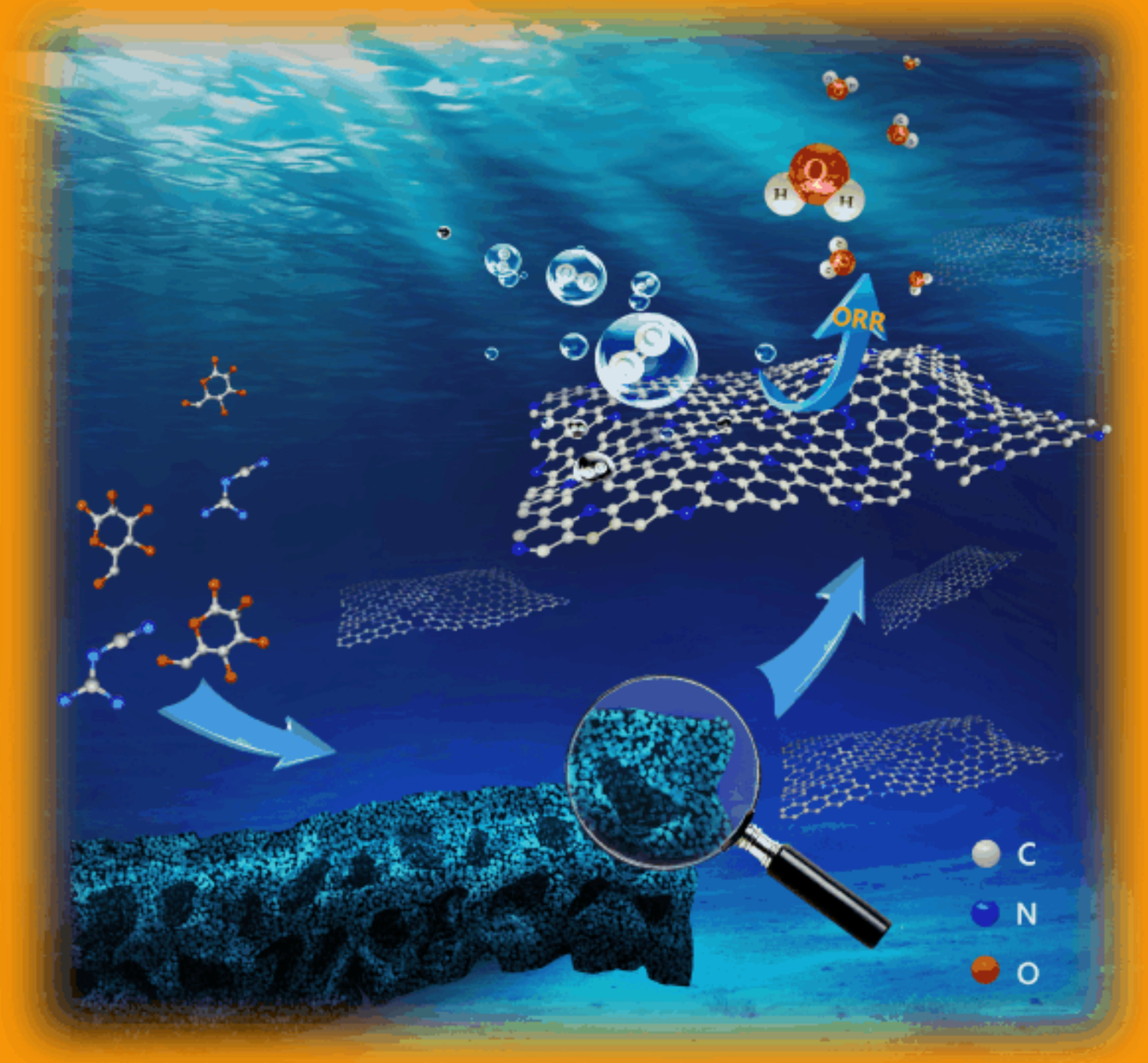

6/2015

A Journal of

ChemPubSoc Europe

A synthetic method is developed for the preparation of N-doped porous carbon through hydrothermal treatment at controlled temperatures, using glucose and dicyandiamide as precursors, and $ZnCl_2$ as an activation reagent. The samples exhibit remarkable catalytic activity in the oxygen reduction reaction (ORR) in alkaline media, comparable to that of state-of-the-art Pt/C catalysts, as discussed by L. Li, S. Chen et al. on p. 803.

www.chemelectrochem.org

WILEY-VCH

ChemPubSoc Europe

DOI: 10.1002/celc.201500002

CHEMELECTROCHEM Articles

High-Performance Electrocatalysts for Oxygen Reduction Based on Nitrogen-Doped Porous Carbon from Hydrothermal Treatment of Glucose and Dicyandiamide

Xiaojun Liu,[a] Ligui Li,*[a] Weijia Zhou,[a] Yucheng Zhou,[a] Wenhan Niu,[a] and Shaowei Chen*[a, b]

A synthetic method was developed for the preparation of N-doped porous carbon through hydrothermal treatment at controlled temperatures by using glucose and dicyandiamide as precursors and $ZnCl_2$ as an activation reagent. Nitrogen doping was quantitatively determined by using XPS measurements and identified in the forms of pyridinic, pyrrolic, graphitic, and pyridinic N^+–O^-nitrogen atoms. Further structural analysis by using SEM, TEM, XRD, Raman, FTIR, and BET measurements showed that the N-doped porous carbons exhibited a microcrystalline graphite structure and a high specific surface area up to 1000 $m^2 g^{-1}$. Electrochemical studies showed that the samples all exhibited a remarkable ORR catalytic activity in alkaline media, which was comparable to that of state-of-the-art Pt/C catalysts, and the one prepared at 800 °C was found to be the best among the series with an onset potential of +0.96 V, almost complete reduction of oxygen to OH^-, and superior methanol tolerance and cycling stability.

1. Introduction

Carbon materials have been used in a wide range of applications, for instance, as electrodes, electrocatalysts, or electrocatalyst supports in energy-storage and -conversion devices,[1–6] because of low costs, high electrical conductivity, chemical inertness, and thermal stability.[7–9] Among the various carbon materials, nitrogen-doped carbon is of particular interest because it exhibits excellent electrocatalytic activity in the oxygen reduction reaction (ORR),[10–15] which is a key reaction at fuel-cell cathodes. For instance, Gong et al.[16] reported that N-doped carbon nanotube arrays acted as efficient metal-free electrocatalysts for oxygen reduction in alkaline media with a performance even better than that of commercial platinum catalysts. Remarkable activity has also been observed with other N-doped carbon catalysts that are based on carbon nanotubes,[16,17] graphene,[18,19] and porous carbon.[20] Of these, N-doped porous carbons have been attracting considerable attention for their high activity and long-term stability. For instance, Asefa and co-workers[21] synthesized N-doped porous carbons by polymerizing polyamine in situ within the pores of SBA-15 mesoporous silica. The doping of N atoms enhanced the ORR activity with an increased current density and decreased overpotential compared to commercial Pt/C catalysts. Yang et al.[22] prepared N-doped porous carbon through the carbonization of nucleobases in an all-organic ionic liquid (1-ethyl-3-methylimidazolium dicyanamide), which showed a high surface area and an ORR performance that was almost identical to that of commercial 20 wt% Pt/C catalysts. At least two critical factors have been identified to account for the high ORR performance of these heteroatom-doped carbon catalysts, 1) elemental composition and interactions between the components, which determine the intrinsic nature of the active sites, and 2) specific surface area and porous structure, which determine accessible active sites and transport properties of ORR-relevant species.

However, to the best of our knowledge, the preparation of high-performance N-doped porous carbon materials for the ORR, as mentioned above, usually requires hard templates to guide and control the formation of mesopores, which inevitably involve several complicated and tedious processes, such as synthesis of monodispersed templating nanoparticles, delicate control over the dispersion of template nanoparticles in carbon matrix, subsequent purification, leaching, and so on. Consequently, many previously reported methods are not beneficial for scale-up production and cost reduction. Therefore, explorations of novel and facile methods for the preparation of N-doped porous carbon catalysts without the aid of commonly used hard templates, such as carbon nanotubes, graphene, silica nanoparticles, and so forth, is still highly in demand. This is the primary motivation of the present work.

In this study, we developed a new and facile hydrothermal method to prepare uniform N-doped carbon spheres (THNC) by using glucose and dicyandiamide as precursors. These were then activated by $ZnCl_2$ at an elevated temperature, ranging

[a] X. Liu, Dr. L. Li, Dr. W. Zhou, Y. Zhou, W. Niu, Prof. Dr. S. Chen
New Energy Research Institute, School of Environment and Energy
South China University of Technology
Guangzhou Higher Education Mega Center, Guangzhou 510006 (China)
E-mail: esguili@scut.edu.cn
shaowei@ucsc.edu

[b] Prof. Dr. S. Chen
Department of Chemistry and Biochemistry, University of California
1156 High Street, Santa Cruz, California 95064 (USA)

Supporting Information for this article is available on the WWW under http://dx.doi.org/10.1002/celc.201500002.

from 700 to 900 °C, in a nitrogen atmosphere to obtain N-doped porous carbon (THNC-T with T being 700, 800, or 900 °C), as manifested in scanning/transmission electron microscopic measurements. XPS measurements showed that the porous carbon was largely graphitic in nature and the level of nitrogen doping decreased with increasing heating temperature, from 5.21% at 700 °C to 4.88% at 800 °C and 3.52% at 900 °C. Nitrogen adsorption/desorption measurements showed that the resultant porous carbon exhibited a high specific surface area and rich porosity. Electrochemical studies showed that the nitrogen-doped porous carbon exhibited a high catalytic activity and stability for ORR, as compared to the commercial 20 wt% Pt/C catalyst.

2. Results and Discussion

In the present study, carbon microspheres were first prepared hydrothermally by using glucose as the carbon precursors[23] and dicyandiamide as the nitrogen source.[24] Subsequent calcination of the resulting carbon microspheres at elevated temperatures led to the production of highly porous N-doped carbon, where $ZnCl_2$ was used as the activating reagent, as $ZnCl_2$ has been known not only to act as a structural template, but also to selectively strip away hydrogen and oxygen atoms in the source materials as water rather than as hydrocarbons or as oxygenated organic compounds and, hence, facilitate the formation of porous carbon.[25,26] The morphology of the porous carbons was first characterized by using field-emission SEM (FESEM) measurements. From the SEM image in Figure 1a,

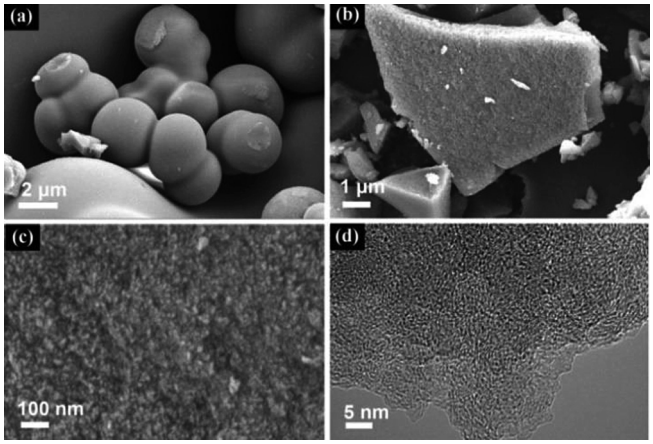

Figure 1. Representative SEM micrographs of a) carbon microspheres prior to $ZnCl_2$ activation (THNC) and b,c) N-doped porous carbon prepared at 800 °C (THNC-800). d) Representative TEM image of THNC-800.

one can see that prior to $ZnCl_2$ activation, the carbon spheres (THNC) exhibited a clean and smooth surface with a diameter of 2–3 μm. In contrast, after thermal activation treatment at 700, 800, and 900 °C (Figure 1b, Figure 1c, and Figures S1a–d), the sphere-like microstructures disappeared and the samples became irregular in shape with a rather rough surface. Furthermore, TEM images (Figure 1d and Figures S1e and f) showed sheet-like structures, which featured small crystalline domains with lattice spacings of about 0.35 nm, suggesting the formation of graphene nanosheets.

This was further confirmed by XRD measurements, as depicted in Figure 2. It can be seen that for the THNC-700 (red curve), THNC-800 (blue curve), and THNC-900 (green curve)

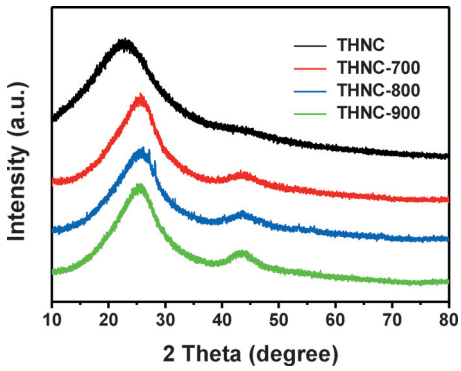

Figure 2. XRD patterns of THNC, THNC-700, THNC-800, and THNC-900 samples.

samples, two peaks emerged at around 25.3 and 43.3°, which are consistent with the (002) and (101) crystalline planes of hexagonal carbon materials (JCPDS, Card No. 75–1621), respectively. In contrast, for the carbon spheres (THNC) prior to $ZnCl_2$ activation, only a single broad peak was observed at a somewhat lower angle of 23.8°, and the peak at 43.3° was too weak to identify (black curve), suggesting that heating at elevated temperatures (700–900 °C) decreased the interlayer spacing between the (002) planes, which is likely caused by the removal of oxygenated species and other structural defects. That is, calcination at elevated temperatures led to enhanced crystallinity and (partial) restoration of the sp^2-hybridized domains, as manifested by the diminishing peak width and slight increase of the diffraction peak positions after heating (Table S1).

The structures of the porous carbons were further examined by Raman spectroscopic measurements, as depicted in Figure 3. It can be seen that THNC, THCN-700, THCN-800, and THNC-900 all show very similar patterns with two broad peaks, that is, a D band at 1350 cm^{-1} and a G band at 1580 cm^{-1}

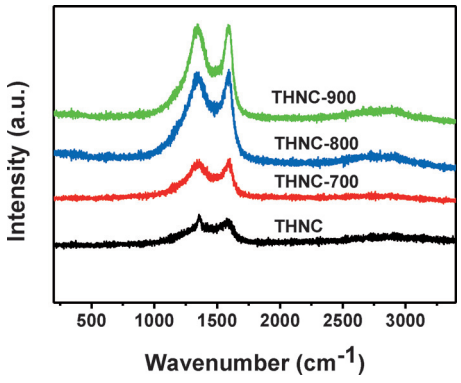

Figure 3. Raman spectra of THNC, THNC-700, THNC-800, and THNC-900 samples.

(Table S2). The former is associated with the vibrations of carbon atoms with dangling bonds in plane terminations of disordered graphite and is related to defects and disorders of structures in carbon materials, whereas the latter is attributed to the vibration of sp^2-bonded carbon in a 2D hexagonal lattice, namely, the stretching modes of C=C bonds of typical graphite.[27] However, the intensities of these two bands varied. Note that the ratio of the D and G band intensities (I_D/I_G) may be exploited for a quantitative assessment of the defect concentration within carbon materials.[28] One can see that, with increasing calcination temperature, the I_D/I_G value decreased slightly, 1.10 (THNC) > 1.07 (THNC-700) > 1.05 (THNC-800) > 1.02 (THNC-900), suggesting a decline in structural defects within the porous carbons at increasing temperatures, which is in good agreement with the XRD results shown in Figure 2.

Further structural insights were obtained in FTIR measurements, which are displayed in Figure 4. One can see that, for THNC, three major vibrational bands appeared at 2960, 2924, and 2868 cm^{-1}. These may be assigned to the C–H stretching

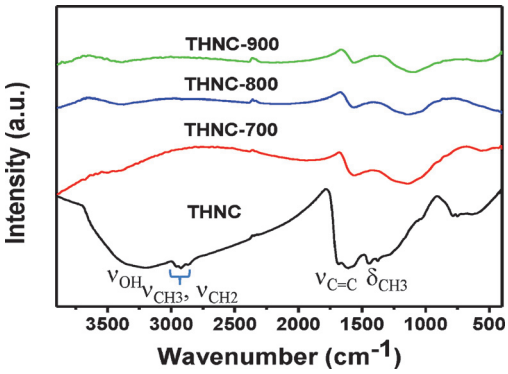

Figure 4. FTIR transmittance spectra of THNC, THNC-700, THNC-800 and THNC-900 samples.

vibrations of CH_2 and CH_3 groups. Another peak emerged at 1380 cm^{-1}, which is likely caused by C–H bending vibrations in CH_3. However, after pyrolysis at elevated temperatures, these four peaks disappeared, indicating effective removal of these functional moieties from the carbon structures, which is consistent with the XRD and Raman data presented above. Furthermore, the O–H stretching vibration at about 3380 cm^{-1} also decreased significantly in intensity, possibly because of the removal of oxygenated species after pyrolysis that rendered the carbon materials increasingly hydrophobic. The C=C stretching vibrations at 1557–1577 cm^{-1}, however, remained rather prominent for all carbon samples.

XPS characterizations were then performed to analyze the elemental compositions and nitrogen-bonding configurations in the porous carbons. From the survey spectra in Figure 5a, the elements of C, N, and O can be identified clearly in all samples, and based on the integrated peak areas, the samples all showed a high content of carbon (more than 75.5 at%) and the level of total nitrogen doping decreased with increasing heating temperature, from 5.21 at% at 700 °C to 4.88 at% at 800 °C and 3.52 at% at 900 °C (Table S3).[29,30] These are signifi-

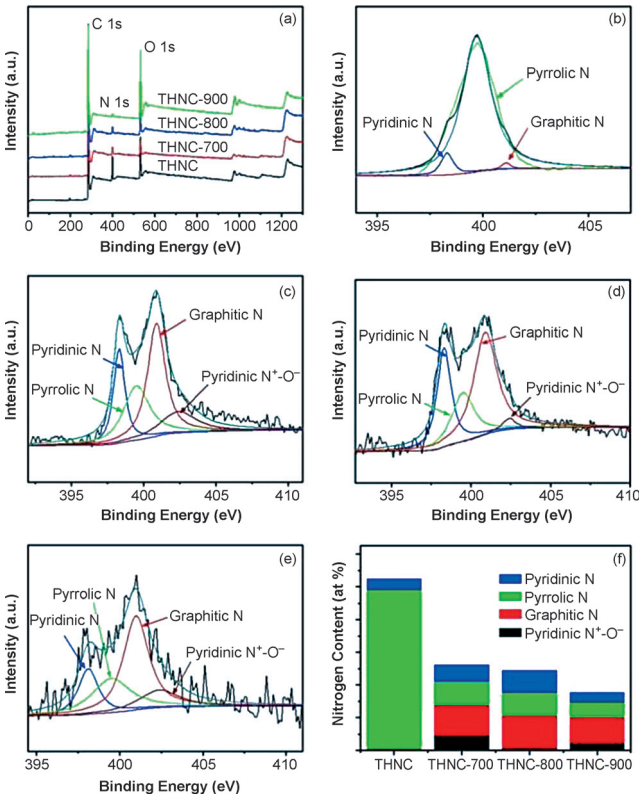

Figure 5. a) XPS survey spectra and high-resolution scans in the N 1s region of b) THNC, c) THNC-700, d) THNC-800, and e) THNC-900. f) Summary of the nitrogen content in the carbon samples.

cantly lower than that (10.5 at%) observed with THNC. Such a changing trend of N content has also been observed in other N-doped carbon materials prepared in a similar fashion, and it is generally attributed to the sequential decomposition of the thermolabile pyrrolic N and pyridinic N^+–O^- species at relatively low pyrolysis temperatures and the degradation of more stable pyridinic N and graphitic N species at higher temperatures[31–35] (trace amounts of $ZnCl_2$ and ZnO can also be observed in the samples, as indicated by the two weak peaks at 1021.9 and 1195.8 eV). In fact, deconvolution of the N 1s peaks in Figures 5b–d yielded four nitrogen-bonding configurations within the samples, that is, pyridinic N at 398.2 eV, pyrrolic N at 399.5 eV, graphitic N at 401.0 eV, and pyridinic oxide (pyridinic N^+–O^-) at 402.4 eV, indicating the successful incorporation of nitrogen dopants within the carbon skeletons.[19,36] Note that, in pre-pyrolysis THNC, pyrrolic N was the dominant species with no pyridinic N^+–O^-;[37] yet after pyrolysis, graphitic N and pyridinic N became the major forms of nitrogen doping and their relative contents increased with increasing calcination temperature. Such a variation in structural composition is summarized in Figure 5f. In particular, in Figure 5f, THNC-800 shows the highest content of pyridinic N (1.36 at%) and graphitic N (1.91 at%), which have been proposed to be primarily responsible for the electrocatalytic activity in ORR.[38–41] In fact, electrochemical studies showed that the THNC-800 samples exhibited the best ORR activity among the series of samples, as detailed below.

Table 1. Summary of specific surface area and pore volumes of nitrogen-doped porous carbons prepared at different temperatures

Sample	S_{BET} [$m^2 g^{-1}$]	Pore volume [$cm^3 g^{-1}$]	Average pore size [nm]
THNC	6.1	–	–
THNC-700	1081.6	0.41	2.77
THNC-800	1036.1	0.53	3.04
THNC-900	1009.8	0.42	2.87

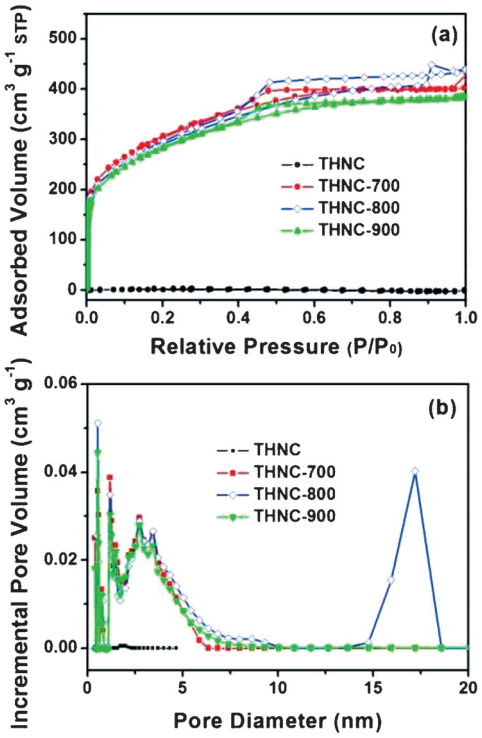

Figure 6. a) Nitrogen adsorption/desorption isotherms and b) pore-size distribution of THNC, THNC-700, THNC-800, and THNC-900.

The specific surface areas of the porous carbons were then quantified by N_2 adsorption/desorption analysis with the results summarized in Table 1. It can be seen from Figure 6a that, prior to $ZnCl_2$ activation, THNC exhibited a very low surface area of only 6.1 $m^2 g^{-1}$ (black curve). This is because the materials were largely nonporous, as manifested in the pore-size distribution in Figure 6b.[42] Yet, after pyrolysis at elevated temperatures, the surface area increased markedly to more than 1000 $m^2 g^{-1}$. Furthermore, one can see that the THNC-700 (red curve), THNC-800 (blue curve), and THNC-900 (green curve) samples all showed a type IV adsorption/desorption isotherm with a clear hysteresis loop in the relative pressure region of $P/P_0 = 0.4–1.0$. This indicates the formation of mesopores in the materials. Consistent results can be seen in the pore-size distribution curves in Figure 6b,[43,44] where micropores below 2 nm and mesopores in the 2–5 nm range can be identified clearly. Importantly, the THNC-800 sample also showed the generation of pores up to 15–18 nm in diameter. It should be noted that high surface areas and unique pore structures are expected to maximize the number of accessible active sites, as well as to facilitate reactant transport inside the materials.

Nitrogen-doped carbon materials such as carbon nanotubes[16] and graphene[19] have been demonstrated to behave as metal-free electrocatalysts that might replace commercial Pt-based catalysts for the ORR. The N-doped porous carbons (THNC-T) prepared above also possessed remarkable electrocatalytic activity for the ORR, as detailed below.

Figure 7a depicts the cyclic voltammograms of a glassy carbon electrode modified with 20 μg of THNC (black curve), THNC-700 (red curve), THNC-800 (blue curve), THNC-900 (green curve), and Pt/C catalysts (magenta curve) in an oxygen-saturated 0.1 M KOH solution at a potential scan rate of 10 $mV s^{-1}$. It can be seen that, for all the carbon samples, non-zero cathodic currents started to emerge at potentials

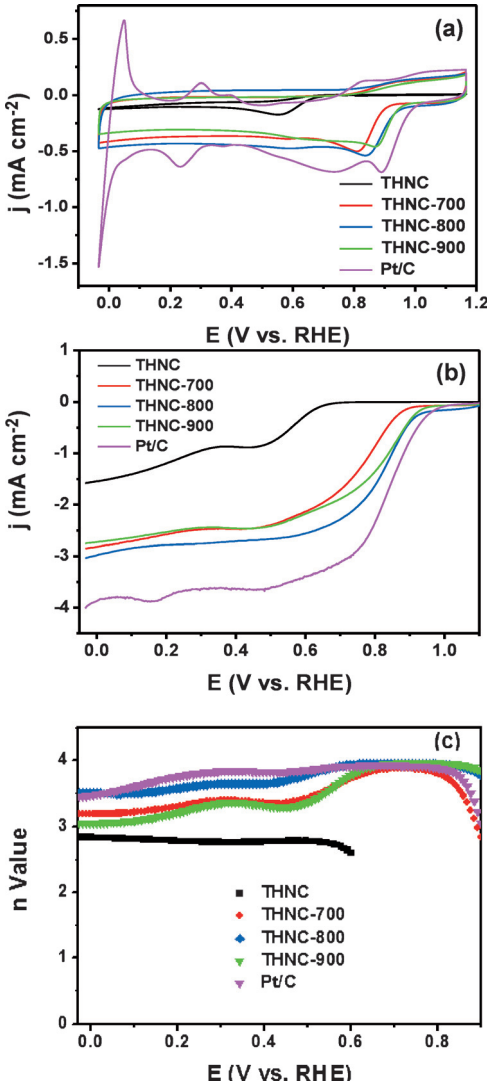

Figure 7. a) Cyclic voltammograms of a glassy carbon electrode modified with 20 μg of THNC, THNC-700, THNC-800, THNC-900, and Pt/C in oxygen-saturated 0.1 M KOH at a scan rate of 10 $mV s^{-1}$. b) RRDE voltammograms of the same electrodes at the rotation rate of 1600 rpm. Scan rate: 10 $mV s^{-1}$. c) Variation of *n* values of THNC, THNC-700, THNC-800, THNC-900, and Pt/C at different potentials.

below +0.95 V and a well-defined peak appeared between +0.8 and +0.9 V, which is in sharp contrast to that observed when the electrolyte solution was saturated with N_2, where the voltammetric profiles were largely featureless and the currents primarily arose from double-layer charging (Figure S2). Similar voltammetric responses were observed with commercial Pt/C catalysts, suggesting apparent ORR activity of the N-doped porous carbon for oxygen reduction. Yet, the electrocatalytic performance is clearly different among the series. For instance, the cathodic peak positions exhibited a clear anodic shift with increasing calcination temperature, that is, +0.55 V for THNC, +0.80 V for THNC-700, +0.85 V for THNC-800, and +0.87 V for THNC-900. Note that the last two are both close to that of commercial Pt/C catalysts (+0.88 V). In addition, the peak current density also exhibited a marked discrepancy at 0.13 mA cm^{-2} for THNC, 0.48 mA cm^{-2} for THNC-700, 0.55 mA cm^{-2} for THNC-800, 0.45 mA cm^{-2} for THNC-900, and 0.64 mA cm^{-2} for Pt/C. Together, these results suggest that 1) thermal treatments at elevated temperatures markedly enhanced the ORR activity of the N-doped porous carbon and 2) 800 °C is the optimal calcination temperature, as the performance of the THNC-800 samples stood out as the best catalysts among the series, which coincided with the highest pyridinic N concentration in THNC-800 among the series (Figure 5)

Further analysis was carried out by using rotating ring-disk electrode (RRDE) voltammetric measurements. Figure 7b shows the RRDE voltammograms of glassy carbon electrodes modified with THNC, THNC-700, THNC-800, THNC-900, and commercial Pt/C at a rotation rate of 1600 rpm in oxygen-saturated 0.1 M KOH. In contrast to THNC, where oxygen reduction did not occur until the electrode potential was below +0.64 V, the porous carbon electrodes all showed much enhanced ORR activity with the onset potentials markedly more positive, that is, +0.92 V for THNC-800 and THNC-900 and +0.88 V for THNC-700, in comparison to +0.95 V for Pt/C. In addition, the limiting diffusion current density at +0.50 V increases in the order of 0.79 mA cm^{-2} (THNC) < 2.40 mA cm^{-2} (THNC-700) < 2.42 mA cm^{-2} (THNC-900) < 2.67 mA cm^{-2} (THNC-800) < 3.62 mA cm^{-2} (Pt/C). These results suggest again that the THNC-800 sample is the best catalysts among the series, although the performance was somewhat subpar compared to commercial Pt/C catalysts.

Furthermore, based on the RRDE measurements (Figure S3), the electron-transfer number (n) during oxygen reduction can be estimated by using Equation (1):[45]

$$n = \frac{4I_{Disk}}{I_{Disk} + I_{Ring}/N} \quad (1)$$

where I_{Disk} represents the disk current, I_{Ring} is the ring current, and N is the RRDE collection efficiency (37%). Figure 7c displays the variation of the electron-transfer number with the potential for the varied carbon catalysts. For THNC, the n values varied slightly from 2.6 to 2.8 within the potential range of 0 to +0.6 V, indicating that oxygen was reduced primarily to peroxide species. Markedly higher n values can be seen with the porous carbons in the same potential ranges [3.2–3.6 (THNC-700), 3.5–3.9 (THNC-800), and 3.0–3.6 (THNC-900)], which were all comparable to that of commercial Pt/C (3.5–3.9), suggesting that the ORR largely proceeded via the four-electron route and OH^- was the primary products of oxygen reduction. For instance, at +0.6 V, the fraction of peroxide intermediates generated decreased in the order of 60% (THNC) > 20% (THNC-700 and THNC-900) > 5% (THNC-800 and Pt/C), again suggesting an optimal heating temperature of 800 °C.

The electron-transfer kinetics involved were then analyzed and quantified by using the Koutecky–Levich method, as the disk currents (J) might include both kinetic- (J_k) and diffusion-controlled (J_d) contributions [Eqs. (2) and (3)]:

$$\frac{1}{J} = \frac{1}{J_k} + \frac{1}{J_d} = \frac{1}{J_k} + \frac{1}{B\omega^{0.5}} \quad (2)$$

$$B = 0.62nFD^{2/3}\nu^{-1/6}C_{O_2} \quad (3)$$

where n is the number of electrons transferred in the oxygen reduction, F is the Faraday constant (96485 C mol^{-1}), ν is the kinematic viscosity of the electrolyte (1.13×10^{-2} cm^2 s^{-1}), D is the oxygen diffusion coefficient (1.9×10^{-5} cm^2 s^{-1}), and C_{O_2} is the oxygen concentration (1.2×10^{-3} M).[46] As shown in Figure S4, for all samples in the series, the Koutecky–Levich plots (J^{-1} vs. $\omega^{-1/2}$) at different electrode potentials displayed good linearity with a rather consistent slope, suggesting a first-order reaction with respect to the concentration of oxygen dissolved in the solution. Furthermore, the corresponding kinetic current density (J_k) can be quantified from the y-axis intercepts by linear regressions, which are depicted in the Tafel plot of Figure 8. It can be seen that all samples exhibited a clear increase in the kinetic current density with increasingly negative electrode potentials. Yet, the activity was clearly different. For instance, the kinetic current density at +0.80 V is 2.42 mA cm^{-2} for THNC-800, which is markedly higher than that for THNC-900 (2.15 mA cm^{-2}) and more than twice that of THNC-700 (1.14 mA cm^{-2}). Note that, at this potential, the ORR activity

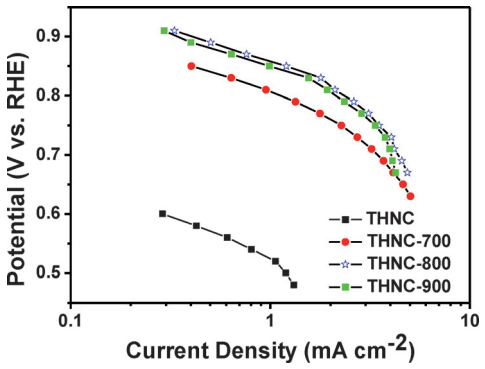

Figure 8. Tafel plots of THNC, THNC-700, THNC-800, and THNC-900. Symbols are experimental data acquired from linear regressions of the Koutecky–Levich plots in Figure S4.

was minimal for THNC. In addition, it can be seen that the Tafel plots demonstrated two distinct segments at low and high overpotentials. In the low overpotential region, linear regressions yielded a slope of 58.3 mV dec^{-1} for THNC-700, 50.1 mV dec^{-1} for THNC-800, and 51.7 mV dec^{-1} for THNC-900. This suggests that, at these N-doped porous carbon catalysts, a pseudo-two-electron reaction was likely to be the rate-determining step in the electrocatalytic reduction of oxygen that followed an outer-sphere electron-transfer pathway.[47–51] In the outer-sphere electron-transfer mechanism, solvated molecular O_2, represented here as a cluster $O_2{\cdot}(H_2O)_n$, might interact with surface adsorbed hydroxyl species (OH_{ads}) through a two-electron reduction pathway to form HO_2^- anions. These reaction intermediates were then further reduced with two additional electrons to OH^- on the active sites or desorbed from the disk electrode surface and eventually detected at the ring electrode, giving rise to a non-zero ring current. This reaction mechanism may be summarized by Equations (4)–(7):

$$C_xN_y^- - OH + [O_2 \bullet (H_2O)_n]_{aq} + e \rightarrow C_xN_y - OH + (HO_2\bullet)_{ads} + OH^- + (H_2O)_{n-1} \quad (4)$$

$$(HO_2\bullet)_{ads} + e^- \rightarrow (HO_2^-)_{ads} \quad (5)$$

$$(HO_2^-)_{ads} \rightarrow (HO_2^-)_{aq} \quad (6)$$

$$(HO_2^-)_{ads} + H_2O + 2e^- \rightarrow 3OH^- \quad (7)$$

where C_xN_y denotes N-doped carbon (primarily pyridinic N and graphitic N sites). In light of the outer-sphere electron-transfer mechanism, it should be noted that, in 0.1 M KOH, the electron-transfer reactions may occur only at active sites. Thus, considering the similar chemical compositions of the porous carbon samples, the best ORR catalytic activity of THNC-800 among the series may be attributed to the relatively high content of pyridinic N (1.36 at%) and graphitic N (1.91 at%) species,[52–54] with additional contributions from the high specific surface area and unique pore architectures that allowed for highly accessible active sites and facilitated mass transport of reactants and products.

The durability of THNC-800 and Pt/C catalysts towards the ORR was then evaluated by using chronoamperometric measurements at +0.4 V and a rotation speed of 900 rpm in a 0.1 M KOH solution saturated with O_2. As shown in Figure 9a, after more than 8 h continuous operation, the cathodic current of the THNC-800 catalyst exhibited only a 5.6% loss, whereas a 17.8% loss was observed with the Pt/C catalysts. This signified markedly better stability of the THNC-800 catalyst than that of commercial Pt/C in alkaline solution.

The THNC-800 catalysts also exhibited significantly enhanced tolerance against methanol crossover, as compared to Pt/C. From Figure 9b, one can see that upon the addition of 3 M methanol into the electrolyte, the ORR current at the Pt/C catalyst suffered a sharp decrease of about 60% in relative current, whereas THNC-800 retained a virtually invariant current response.

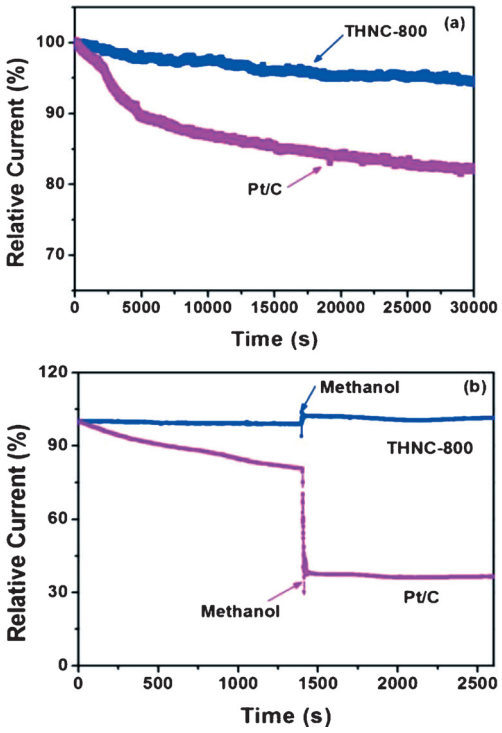

Figure 9. a) Chronoamperometric profiles of THNC-800 and Pt/C electrodes in O_2-saturated 0.1 M KOH at +0.40 V for 30 000 s. b) Chronoamperometric responses of THNC-800 and Pt/C electrodes with the addition of 3 M methanol.

3. Conclusions

N-doped porous carbon was prepared through a simple hydrothermal procedure at controlled temperatures (700–900 °C) by using glucose and dicyanamide as the precursors and $ZnCl_2$ as the activation reagent. The porosity was quantified in nitrogen adsorption/desorption measurements that signified the formation of a mesoporous structure with a BET specific surface area more than 1000 m^2 g^{-1}. Nitrogen doping was then examined through XPS measurements and four nitrogen-bonding configurations were identified and quantified, including pyridinic, pyrrolic, graphitic, and pyridinic N^+–O^-. Electrochemical studies showed that the porous carbon exhibited apparent electrocatalytic activity in oxygen reduction in alkaline media, with a performance comparable to that of the state-of-art Pt/C catalysts, within the context of onset potential, number of electron transfer, as well as kinetic current density, methanol tolerance, and durability. In particular, the best performance was observed with the samples prepared at a heating temperature of 800 °C. This might be ascribed to the high doping of pyridinic and graphitic nitrogen species that were primarily responsible for the ORR activity and the unique mesoporous structure that facilitated accessibility of the catalytically active sites and mass transport of ORR reactants and products. The results presented herein may offer a new and effective strategy for the preparation and engineering of metal-free all-carbon-based catalysts for oxygen reduction.

Experimental Section

Synthesis of N-Doped Porous Carbon

In a typical experiment, an aqueous solution (15 mL) containing 0.5 M glucose and 0.25 M dicyandiamide was transferred into a 25 mL Teflon-lined stainless-steel autoclave and statically heated at 200 °C for 24 h. The obtained black precipitates, which were N-doped carbon microspheres (denoted as THNC), were washed with distilled water several times and dried in a vacuum oven at 70 °C for 12 h, followed by chemical activation by heating with $ZnCl_2$ (carbon/$ZnCl_2$ = 1:6, w/w) under N_2 at an elevated temperature (700, 800, or 900 °C) for 2 h at a temperature ramp of 5 °C min^{-1}. The solids were then collected, soaked in 1.0 M HCl for 4 h under ultrasonication, washed extensively with deionized water, and finally dried in a vacuum oven at 70 °C for 12 h, affording N-doped porous carbon, which was denoted as THNC-T (with T being the temperature at which the sample was prepared).

Characterization

The morphology was examined with a field-emission scanning electron microscope (Zeiss) and a high-resolution transmission electron microscope (JEOL JEM-2010). Nitrogen adsorption and desorption measurements were performed at 77 K with a Micromeritics ASAP 2020 analyzer. The specific surface area (S_{BET}) was calculated by the conventional BET (Brunauer–Emmett–Teller) method. The total pore volume (V_t) was calculated from the adsorbed N_2 amount at a relative pressure of $P/P_0 = 0.99$. The pore-size distribution was calculated with a density function theory (DFT) method by using the nitrogen adsorption data and assuming a slit pore model. XRD patterns in the Bragg's angle (2θ) range of 10–80° were collected at room temperature by using a Bruker D_8 diffractometer with CuK_α radiation ($\lambda = 0.1541$ nm). Raman spectra were acquired by using a Lab RAMARAMIS (Horiba JobinYvon) instrument equipped with a 50 mW He–Ne laser at 532 nm and a charge-coupled device (CCD) detector. FTIR measurements were performed at ambient temperature with a Nicolet 6700 FTIR spectrometer. XPS analysis was carried out with a VG MultiLab 2000 instrument with a monochromatic AlK_α X-ray source (Thermo VG Scientific).

Electrochemistry

Voltammetric measurements of the ORR activity were conducted in a three-electrode system by using a CHI 660E electrochemical workstation. A Pt foil and a reversible hydrogen electrode (RHE) were used as the counter electrode and reference electrode, respectively. The working electrode was a glassy carbon-disk electrode (diameter 5.61 mm) of a RRDE (with a collection efficiency of 37%) from Pine Instrument, Inc.[55] The working electrode was polished sequentially with aqueous slurries of 0.3, 0.1, and 0.05 μm alumina powders on a polishing microcloth. The carbon samples (2 mg) were ultrasonically dispersed in ethanol solution (1.0 mL) containing Nafion (5 wt%, Aldrich) for 30 min to form a homogenous catalyst ink. The catalyst ink (10 μL) was drop-cast onto the glassy carbon disk, followed by drying at room temperature. Commercial Pt/C was loaded onto the electrode surface in a similar fashion. In this study, the loadings of the catalysts were all 20 μg. Electrochemical measurements were performed at room temperature in 0.1 M KOH solutions and the geometrical surface area of the electrode was used to calculate the current density.

Acknowledgements

This work was supported by the National Recruitment Program of Global Experts. L.G.L acknowledges financial support from the Fundamental Research Funds for the Central Universities (Grant No. 2013M0019). S.W.C. acknowledges support from the National Science Foundation (CHE-1265635 and DMR-1409396).

Keywords: dicyandiamide · glucose · oxygen reduction · porous carbons · pyrolysis

[1] J. Biener, M. Stadermann, M. Suss, M. A. Worsley, M. M. Biener, K. A. Rose, T. F. Baumann, *Energy Environ. Sci.* **2011**, *4*, 656–667.
[2] S. L. Candelaria, Y. Shao, W. Zhou, X. Li, J. Xiao, J.-G. Zhang, Y. Wang, J. Liu, J. Li, G. Cao, *Nano Energy* **2012**, *1*, 195–220.
[3] Y. Zhou, K. Neyerlin, T. S. Olson, S. Pylypenko, J. Bult, H. N. Dinh, T. Gennett, Z. Shao, R. O'Hayre, *Energy Environ. Sci.* **2010**, *3*, 1437–1446.
[4] G. Lota, K. Fic, E. Frackowiak, *Energy Environ. Sci.* **2011**, *4*, 1592–1605.
[5] Y.-S. Hu, R. Demir-Cakan, M.-M. Titirici, J.-O. Müller, R. Schlögl, M. Antonietti, J. Maier, *Angew. Chem. Int. Ed.* **2008**, *47*, 1645–1649; *Angew. Chem.* **2008**, *120*, 1669–1673.
[6] Q. Li, R. Cao, J. Cho, G. Wu, *Adv. Energy Mater.* **2014**, *4*, 1301415.
[7] B. Fang, J. H. Kim, M.-S. Kim, J.-S. Yu, *Acc. Chem. Res.* **2013**, *46*, 1397–1406.
[8] Y. Zhu, L. Li, C. Zhang, G. Casillas, Z. Sun, Z. Yan, G. Ruan, Z. Peng, A.-R. O. Raji, C. Kittrell, R. H. Hauge, J. M. Tour, *Nat. Commun.* **2012**, *3*, 1225.
[9] A. K. Geim, *Science* **2009**, *324*, 1530–1534.
[10] N. Brun, S. A. Wohlgemuth, P. Osiceanu, M. M. Titirici, *Green Chem.* **2013**, *15*, 2514–2524.
[11] S. Gao, H. Fan, Y. Chen, L. Li, Y. Bando, D. Golberg, *Nano Energy* **2013**, *2*, 1261–1270.
[12] J. Duan, Y. Zheng, S. Chen, Y. Tang, M. Jaroniec, S. Qiao, *Chem. Commun.* **2013**, *49*, 7705–7707.
[13] J. Jin, X. Fu, Q. Liu, J. Zhang, *J. Mater. Chem. A* **2013**, *1*, 10538–10545.
[14] R. Zhang, W. Chen, *J. Mater. Chem. A* **2013**, *1*, 11457–11464.
[15] S. Yasuda, L. Yu, J. Kim, K. Murakoshi, *Chem. Commun.* **2013**, *49*, 9627–9629.
[16] K. Gong, F. Du, Z. Xia, M. Durstock, L. Dai, *Science* **2009**, *323*, 760–764.
[17] S. Ratso, I. Kruusenberg, M. Vikkisk, U. Joost, E. Shulga, I. Kink, T. Kallio, K. Tammeveski, *Carbon* **2014**, *73*, 361–370.
[18] S. Niyogi, E. Bekyarova, M. E. Itkis, J. L. McWilliams, M. A. Hamon, R. C. Haddon, *J. Am. Chem. Soc.* **2006**, *128*, 7720–7721.
[19] L. Qu, Y. Liu, J.-B. Baek, L. Dai, *ACS Nano* **2010**, *4*, 1321–1326.
[20] W. Wei, H. Liang, K. Parvez, X. Zhuang, X. Feng, K. Müllen, *Angew. Chem. Int. Ed.* **2014**, *53*, 1570–1574; *Angew. Chem.* **2014**, *126*, 1596–1600.
[21] R. Silva, D. Voiry, M. Chhowalla, T. Asefa, *J. Am. Chem. Soc.* **2013**, *135*, 7823–7826.
[22] W. Yang, T.-P. Fellinger, M. Antonietti, *J. Am. Chem. Soc.* **2011**, *133*, 206–209.
[23] H. T. Li, X. D. He, Y. Liu, H. Huang, S. Y. Lian, S. T. Lee, Z. H. Kang, *Carbon* **2011**, *49*, 605–609.
[24] Q. Li, P. Xu, W. Gao, S. G. Ma, G. Q. Zhang, R. G. Cao, J. Cho, H. L. Wang, G. Wu, *Adv. Mater.* **2014**, *26*, 1378–1386.
[25] Z. Hu, M. P. Srinivasan, Y. Ni, *Carbon* **2001**, *39*, 877–886.
[26] X. He, P. Ling, M. Yu, X. Wang, X. Zhang, M. Zheng, *Electrochim. Acta* **2013**, *105*, 635–641.
[27] Y. Zhou, Q. Bao, L. A. L. Tang, Y. Zhong, K. P. Loh, *Chem. Mater.* **2009**, *21*, 2950–2956.
[28] Y. Zhang, K. Fugane, T. Mori, L. Niu, J. Ye, *J. Mater. Chem.* **2012**, *22*, 6575–6580.
[29] G. Wu, N. H. Mack, W. Gao, S. G. Ma, R. Q. Zhong, J. T. Han, J. K. Baldwin, P. Zelenay, *ACS Nano* **2012**, *6*, 9764–9776.
[30] G. Wu, C. M. Johnston, N. H. Mack, K. Artyushkova, M. Ferrandon, M. Nelson, J. S. Lezama-Pacheco, S. D. Conradson, K. L. More, D. J. Myers, P. Zelenay, *J. Mater. Chem.* **2011**, *21*, 11392–11405.

[31] J. R. Pels, F. Kapteijn, J. A. Moulijn, Q. Zhu, K. M. Thomas, *Carbon* **1995**, *33*, 1641 – 1653.
[32] Z. Lei, M. Zhao, L. Dang, L. An, M. Lu, A.-Y. Lo, N. Yu, S.-B. Liu, *J. Mater. Chem.* **2009**, *19*, 5985 – 5995.
[33] E. Proietti, F. Jaouen, M. Lefèvre, N. Larouche, J. Tian, J. Herranz, J.-P. Dodelet, *Nat. Commun.* **2011**, *2*, 416.
[34] X. She, D. Yang, D. Jing, F. Yuan, W. Yang, L. Guo, Y. Che, *Nanoscale* **2014**, *6*, 11057 – 11061.
[35] R. Liu, D. Wu, X. Feng, K. Müllen, *Angew. Chem. Int. Ed.* **2010**, *49*, 2565 – 2569; *Angew. Chem.* **2010**, *122*, 2619 – 2623.
[36] Z.-H. Sheng, L. Shao, J.-J. Chen, W.-J. Bao, F.-B. Wang, X.-H. Xia, *ACS Nano* **2011**, *5*, 4350 – 4358.
[37] Z. Chen, D. Higgins, H. Tao, R. S. Hsu, Z. Chen, *J. Phys. Chem. C* **2009**, *113*, 21008 – 21013.
[38] D. Geng, Y. Chen, Y. Chen, Y. Li, R. Li, X. Sun, S. Ye, S. Knights, *Energy Environ. Sci.* **2011**, *4*, 760 – 764.
[39] W. Ding, Z. Wei, S. Chen, X. Qi, T. Yang, J. Hu, D. Wang, L.-J. Wan, S. F. Alvi, L. Li, *Angew. Chem. Int. Ed.* **2013**, *52*, 11755 – 11759; *Angew. Chem.* **2013**, *125*, 11971 – 11975.
[40] B. Zhang, Z. Wen, S. Ci, S. Mao, J. Chen, Z. He, *ACS Appl. Mater. Interfaces* **2014**, *6*, 7464 – 7470.
[41] L. Lai, J. R. Potts, D. Zhan, L. Wang, C. K. Poh, C. Tang, H. Gong, Z. Shen, J. Lin, R. S. Ruoff, *Energy Environ. Sci.* **2012**, *5*, 7936 – 7942.
[42] Q. Zhao, T.-P. Fellinger, M. Antonietti, J. Yuan, *J. Mater. Chem. A* **2013**, *1*, 5113 – 5120.
[43] L. Qie, W.-M. Chen, Z.-H. Wang, Q.-G. Shao, X. Li, L.-X. Yuan, X.-L. Hu, W.-X. Zhang, Y.-H. Huang, *Adv. Mater.* **2012**, *24*, 2047 – 2050.
[44] M. Armandi, B. Bonelli, F. Geobaldo, E. Garrone, *Microporous Mesoporous Mater.* **2010**, *132*, 414 – 420.
[45] K. Parvez, S. Yang, Y. Hernandez, A. Winter, A. Turchanin, X. Feng, K. Müllen, *ACS Nano* **2012**, *6*, 9541 – 9550.
[46] R. E. Davis, G. L. Horvath, C. W. Tobias, *Electrochim. Acta* **1967**, *12*, 287 – 297.
[47] K. Zhou, W. Zhou, X. Liu, Y. Wang, J. Wan, S. Chen, *ACS Appl. Mater. Interfaces* **2014**, *6*, 14911 – 14918.
[48] C. Zhang, F.-R. F. Fan, A. J. Bard, *J. Am. Chem. Soc.* **2009**, *131*, 177 – 181.
[49] W. Y. Wong, W. R. W. Daud, A. B. Mohamad, A. A. H. Kadhum, K. S. Loh, E. H. Majlan, K. L. Lim, *Electrochim. Acta* **2014**, *129*, 47 – 54.
[50] N. Ramaswamy, S. Mukerjee, *J. Phys. Chem. C* **2011**, *115*, 18015 – 18026.
[51] P. Esakki Karthik, C. Jeyabharathi, K. L. Phani, *Chem. Commun.* **2014**, *50*, 2787 – 2790.
[52] H. Kim, K. Lee, S. I. Woo, Y. Jung, *Phys. Chem. Chem. Phys.* **2011**, *13*, 17505 – 17510.
[53] L. Zhang, Z. Su, F. Jiang, L. Yang, J. Qian, Y. Zhou, W. Li, M. Hong, *Nanoscale* **2014**, *6*, 6590 – 6602.
[54] N. Daems, X. Sheng, I. F. J. Vankelecom, P. P. Pescarmona, *J. Mater. Chem. A* **2014**, *2*, 4085 – 4110.
[55] Z.-Y. Zhou, X. Kang, Y. Song, S. Chen, *Chem. Commun.* **2012**, *48*, 3391 – 3393.

Received: January 2, 2015
Revised: January 30, 2015
Published online on March 4, 2015